Dependence of Simulation Biases at AHI Surface-Sensitive Channels on Land Surface Emissivity over China

X. ZHUGE

School of Atmospheric Sciences, and Key Laboratory of Mesoscale Severe Weather, Ministry of Education, Nanjing University, Nanjing, China, and Earth System Science Interdisciplinary Center, University of Maryland, College Park, College Park, Maryland

X. ZOU

Earth System Science Interdisciplinary Center, University of Maryland, College Park, College Park, Maryland

F. WENG

NOAA/Center for Satellite Applications and Research, College Park, Maryland

M. SUN

School of Atmospheric Sciences, and Key Laboratory of Mesoscale Severe Weather, Ministry of Education, Nanjing University, Nanjing, and Shanghai Central Meteorological Observatory, Shanghai, China

(Manuscript received 4 September 2017, in final form 27 March 2018)

ABSTRACT

This study compares the simulation biases of Advanced Himawari Imager (AHI) brightness temperature to observations made at night over China through the use of three land surface emissivity (LSE) datasets. The University of Wisconsin–Madison High Spectral Resolution Emissivity dataset, the Combined Advanced Spaceborne Thermal Emission and Reflection Radiometer and Moderate Resolution Imaging Spectroradiometer Emissivity database over Land High Spectral Resolution Emissivity dataset, and the International Geosphere–Biosphere Programme (IGBP) infrared LSE module, as well as land skin temperature observations from the National Basic Meteorological Observing stations in China are used as inputs to the Community Radiative Transfer Model. The results suggest that the standard deviations of AHI observations minus background simulations (OMBs) are largely consistent for the three LSE datasets. Also, negative biases of the OMBs of brightness temperature uniformly occur for each of the three datasets. There are no significant differences in OMB biases estimated with the three LSE datasets over cropland and forest surface types for all five AHI surface-sensitive channels. Over the grassland surface type, significant differences (~0.8 K) are found at the 10.4-, 11.2-, and 12.4-μm channels if using the IGBP dataset. Over nonvegetated surface types (e.g., sandy land, gobi, and bare rock), the lack of a monthly variation in IGBP LSE introduces large negative biases for the 3.9- and 8.6-μm channels, which are greater than those from the two other LSE datasets. Thus, improvements in simulating AHI infrared surface-sensitive channels can be made when using spatially and temporally varying LSE estimates.

1. Introduction

The infrared imagers on board geostationary satellites provide rich information about the atmosphere and surface through their high temporal and spatial sampling. In particular, infrared measurements are very much needed for nowcasting fast-evolving convective weather systems (Walker et al. 2012; Zhuge and Zou 2018) and for predicting precipitation through radiance assimilation (Zou et al. 2011, 2015; Qin et al. 2017). The infrared radiance at a wavelength λ under clear-sky conditions L_λ can be simulated based on the following emission-based radiative transfer equation (Chen 2005):

Denotes content that is immediately available upon publication as open access.

Corresponding author: Dr. X. Zou, xzou1@umd.edu.

DOI: 10.1175/JTECH-D-17-0152.1

© 2018 American Meteorological Society. For information regarding reuse of this content and general copyright information, consult the AMS Copyright Policy (www.ametsoc.org/PUBSReuseLicenses).

Brought to you by NOAA Central Library | Unauthenticated | Downloaded 01/30/24 04:02 PM UTC

$$L_\lambda = \varepsilon_{\lambda s} B_\lambda(T_s)\tau_\lambda(P_s) + \int_{P_s}^{1} B_\lambda(T)\frac{\partial \tau_\lambda(P)}{\partial P}dP, \qquad (1)$$

where $\varepsilon_{\lambda s}$ is the surface emissivity, T_s is the surface skin temperature, $B_\lambda(T)$ is the Planck function as a function of λ and temperature T, and $\tau_\lambda(P)$ is the transmittance from a pressure layer P to space. Transmittance always has a value because of the existence of water vapor and other absorbers in the atmosphere. Under clear-sky conditions, the bias of simulated infrared radiances to observations is mostly affected by atmospheric temperature and absorber profiles. For infrared surface-sensitive channels where the weighting function $[\partial\tau_\lambda(P)/\partial P]$ is the largest at the surface, the accuracy of radiance simulations is strongly dependent on $\varepsilon_{\lambda s}$ and T_s. As pointed out by Li et al. (2010), a standard deviation error of 0.025 in the surface emissivity at 10.8 μm would lead to an error of ~1.14 K in the simulated brightness temperature at this wavelength.

Although significant progress has been made in infrared radiance data assimilation, surface-sensitive infrared radiance observations over land are currently excluded from data assimilation systems mainly because of the large uncertainties in land surface emissivity (LSE) input into a fast radiative transfer model. Although the land skin temperature (LST) also has large uncertainties over areas with complicated land surface characteristics (Zheng et al. 2012; Trigo et al. 2015; Zhuo et al. 2016), it is not strictly required, since it is often adjusted in the data assimilation process based on the land–atmospheric interaction and radiative balance. To better utilize surface-sensitive infrared radiance data in data assimilation systems over land, highly accurate LSE datasets (e.g., better than 0.08 accuracy) are required.

The Community Radiative Transfer Model (CRTM) is a fast radiative transfer model that is widely used in satellite data assimilation (Han et al. 2007; Weng 2007). Compared to a line-by-line radiative transfer model, the CRTM has a precision better than 0.03 and 0.1 K in the infrared and microwave spectral regions, respectively (Chen et al. 2010). In the current version of the CRTM—that is, CRTM, version 2.2.3 (CRTMv2.2.3)—three infrared LSE modules are used for generating the surface emissivity over land, namely, modules involving LSE datasets from the National Polar-Orbiting Operational Environmental Satellite System, the U.S. Geological Survey, and the International Geosphere–Biosphere Programme (IGBP). Each of these LSE modules consists of a lookup table (LUT) for reflectance as a function of wavenumber and surface type. The surface emissivity is calculated as one minus the reflectance under the assumption of a Lambertian surface (Salisbury et al. 1994). Hence, the accuracy of the LSE module is affected by both the LUTs and the surface type dataset. Vogel et al. (2010) and Zhuge et al. (2017a) have demonstrated that the IGBP module provides a realistic estimate of LSE. However, Zou et al. (2016) showed that CRTM simulations over land deviated greatly from observations made by the Advanced Himawari Imager (AHI) on board the Japanese *Himawari-8* satellite, even if the LSE from the IGBP infrared LSE module (IGBP LSE dataset) was used. Fortunately, the current version of the CRTM accepts a user-defined LSE. In other words, users can dynamically input an external LSE dataset into the CRTM for each observation.

Most of the infrared LSE datasets are retrieved from instruments on board polar-orbiting satellites, such as the Visible Infrared Imaging Radiometer Suite on board the *Suomi National Polar-orbiting Partnership* satellite, the Moderate Resolution Imaging Spectroradiometer (MODIS) on board the *Aqua* and *Terra* satellites, and the Advanced Spaceborne Thermal Emission and Reflection Radiometer (ASTER) on board the *Terra* satellite. Among the different global infrared LSE datasets, the University of Wisconsin–Madison (UW) High Spectral Resolution Emissivity dataset (UW_HSRemis) and the Combined ASTER and MODIS Emissivity over Land (CAMEL) High Spectral Resolution Emissivity dataset (CAMEL_HSRemis) have the best accuracy (Seemann et al. 2008; Borbas et al. 2017).

Through comparisons with AHI observations at the five AHI surface-sensitive channels, we assess the impacts of the IGBP LSE dataset, UW_HSRemis, and CAMEL_HSRemis on CRTM simulations over different surface types. This paper is organized as follows: Section 2 provides a brief description of the LSE datasets, AHI observations, and model simulations. A comparison among the three infrared LSE datasets is made in section 3. The uncertainties of model-forecasted LST are discussed in section 4. Impacts of infrared LSE models on the simulations of AHI surface-sensitive channels are presented in section 5. Summary and conclusions are provided in section 6.

2. Data description

a. High-spectral-resolution LSE

The UW developed a global infrared LSE dataset called the UW Baseline-Fit (UWBF) emissivity dataset (Seemann et al. 2008). The UWBF emissivity dataset is derived from MODIS Land Surface Temperature and Emissivity (MOD11) products. It provides monthly mean global emissivities at 10 wavelengths (3.6, 4.3,

Brought to you by NOAA Central Library | Unauthenticated | Downloaded 01/30/24 04:02 PM UTC

TABLE 1. Central wavelengths, pressures of the peak weighting function (WF), and the biases of AHI infrared channels 7–16 under clear-sky conditions over oceans with respect to model simulations and CrIS observations. The model simulations of brightness temperature are obtained from ECMWF analyses using CRTMv2.2.3.

Channel No.	Central wavelength (μm)	WF peak (hPa)	Bias (K) w.r.t. Simulations	Bias (K) w.r.t. CrIS data
7	3.9	Surface	0.28	−0.059 at 290 K
8	6.2	350	−0.17	−0.150 at 220 K
9	6.9	450	0.44	−0.212 at 250 K
10	7.3	600	−0.34	−0.230 at 250 K
11	8.6	Surface	−0.45	0.231 at 290 K
12	9.6	40	−0.01	−0.117 at 250 K
13	10.4	Surface	−0.30	0.004 at 290 K
14	11.2		−0.26	0.015 at 290 K
15	12.4		−0.56	−0.095 at 290 K
16	13.3	990	−0.52	−0.007 at 290 K

5.0, 5.8, 7.6, 8.3, 9.3, 10.8, 12.1, and 14.3 μm) and at a latitude × longitude spatial resolution of 0.05° × 0.05° from 2003 to 2015. Because MODIS has only three thermal-infrared bands in the 8–12-μm spectral region (8.55, 11, and 12 μm), the emissivity in this spectral region undergoes a form of extrapolation and is thus not well defined in the two quartz doublet regions at 8.5 and 12 μm (Borbas et al. 2017).

The Jet Propulsion Laboratory recently released the fourth version (v4) of the ASTER Global Emissivity Dataset (Hulley et al. 2015). The ASTER Global Emissivity Dataset, v4 provides monthly mean emissivities at only five thermal-infrared wavelengths (8.3, 8.6, 9.1, 10.6, and 11.3 μm) at a latitude × longitude spatial resolution of 0.05° × 0.05° from 2000 to 2015.

A CAMEL emissivity dataset was produced by merging the UWBF Emissivity Dataset with the ASTER Global Emissivity Dataset v4 to capitalize on the unique strengths of each product's characteristics (Borbas et al. 2017). The CAMEL emissivity dataset provides monthly emissivities from 2003 to 2015 at a latitude × longitude spatial resolution of 0.05° × 0.05° for 13 bands within the spectral region of 3.6–14.3 μm (3.6, 4.3, 5, 5.8, 7.6, 8.3, 8.6, 9.1, 10.6, 10.8, 11.3, 12.1, and 14.3 μm).

Both the UWBF and CAMEL emissivity datasets were extended to a high spectral resolution using a principal component regression approach and laboratory-measured emissivity spectra–derived eigenvectors (Borbas et al. 2007; Borbas and Ruston 2010). The UW_HSRemis is generated at 416 wavenumber points within the spectral range from 699.3 to 2774.3 cm^{-1} at a 5 cm^{-1} spectral resolution, while the CAMEL_HSRemis is generated at 417 wavenumber points within the spectral range from 694 to 2778 cm^{-1} at a 5 cm^{-1} spectral resolution. In this study UW_HSRemis and CAMEL_HSRemis in 2015 were used to simulate the brightness temperatures of AHI surface-sensitive channels. A convolution with the spectral response function of AHI was used to obtain emissivities at the five surface-sensitive AHI channels from UW_HSRemis and CAMEL_HSRemis.

b. *AHI observations and simulations*

The AHI/*Himawari-8* satellite is positioned in a geostationary orbit at an altitude of 35 800 km above the equator at 140.7°E (Bessho et al. 2016). It provides a full disk scan of the Eastern Hemisphere every 10 min with a subpoint resolution of 2 km. The AHI has 10 infrared channels, including a stratospheric ozone channel with its wavelength centered at 9.6 μm (channel 12); three water vapor channels centered at 6.2, 6.9, and 7.3 μm (channels 8–10, respectively); a CO_2 channel at 13.3 μm (channel 16); and five surface-sensitive channels with their central wavelengths located at 3.9, 8.6, 10.4, 11.2, and 12.4 μm (channels 7, 11, and 13–15), respectively. The biases for AHI infrared channels with respect to Cross-Track Infrared Sounder (CrIS) observations obtained by Takahashi (2016) are provided in Table 1. The AHI to CrIS biases at 290 K are ~0.23 K for the 8.6-μm channel and less than 0.10 K for the other four surface-sensitive channels (Takahashi 2016), suggesting a high radiometric calibration accuracy of the AHI instrument. Table 1 also provides the biases for AHI infrared channels with respect to model simulations using CRTMv2.2.3 with the European Centre for Medium-Range Weather Forecasts (ECMWF) analyses under clear-sky conditions over oceans. The biases for the five AHI surface-sensitive channels are 0.28, −0.45, −0.30, −0.26, and −0.56 K, respectively (Zou et al. 2016).

In this study the AHI radiance simulations are also calculated using CRTMv2.2.3. The LST measurements serving as inputs to the CRTM are collected hourly

Brought to you by NOAA Central Library | Unauthenticated | Downloaded 01/30/24 04:02 PM UTC

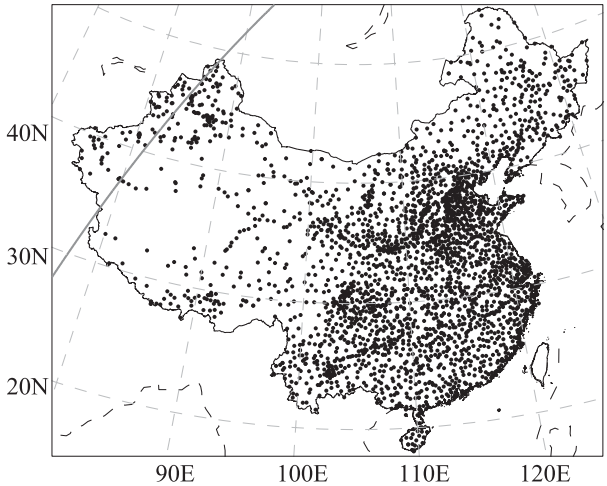

FIG. 1. Spatial distribution of the NBMO stations of China. The satellite zenith angle is 75° at the location marked (solid gray line).

at 2423 National Basic Meteorological Observing (NBMO) stations in China. These NBMO stations are densely distributed in eastern China but sparsely in western China (Fig. 1). There is a strict requirement on the local environment and the observing instruments at these stations. Measurements provided by the NBMO stations in China are thus credible. A spatial consistency test is done to ensure that an LST measurement from a certain station was close to the mean value of its neighboring stations within a 2° × 2° area. Specifically, a gross quality control was applied to remove those LST data that deviated from the mean value by less than −10 K or greater than 20 K. The vertical profiles of atmospheric temperature, water vapor, and ozone serving as inputs to the CRTM are obtained from the National Centers for Environmental Prediction (NCEP) Global Forecast System (GFS) analyses that are available at 6-h intervals. NCEP GFS data are global and have a 0.25° × 0.25° horizontal resolution and 31 vertical levels from the earth's surface to about 1 hPa. In this study we use data observed at 0300, 0900, 1500, and 2100 UTC on 144 days, that is, the 2nd, 7th, 12th, 17th, 22nd, and 27th of each month in the 2-yr period from July 2015 to June 2017. The NCEP GFS grid was interpolated to the NBMO stations using a bilinear interpolation method.

This study focuses on model simulations of AHI surface-sensitive channels under clear-sky conditions. Clear AHI pixels are identified based on the AHI cloud mask that is created using an infrared-only cloud mask algorithm during nighttime (Zhuge and Zou 2016) and a visible-based fast cloud mask algorithm during daytime (Zhuge et al. 2017b). A "probability of correct typing" of 91.94% and 92.59% is achieved over land during daytime and nighttime, respectively, when compared to the MODIS cloud mask product (MYD35). Data with satellite zenith angles greater than 75° are also excluded.

c. *Topography and land-cover datasets*

The topography database with a 1-arc-min resolution is provided by the National Centers for Environmental Information, National Oceanic and Atmospheric Administration (via http://www.ngdc.noaa.gov/mgg/global/global.html). Figure 2a shows the spatial distribution of terrain heights over China. In general, the terrain height is high in western China and low in eastern China. The Tibetan Plateau, where the elevation is greater than 3000 m, is located in southwestern China. Surrounding the Tibetan Plateau are four great basins, namely, the

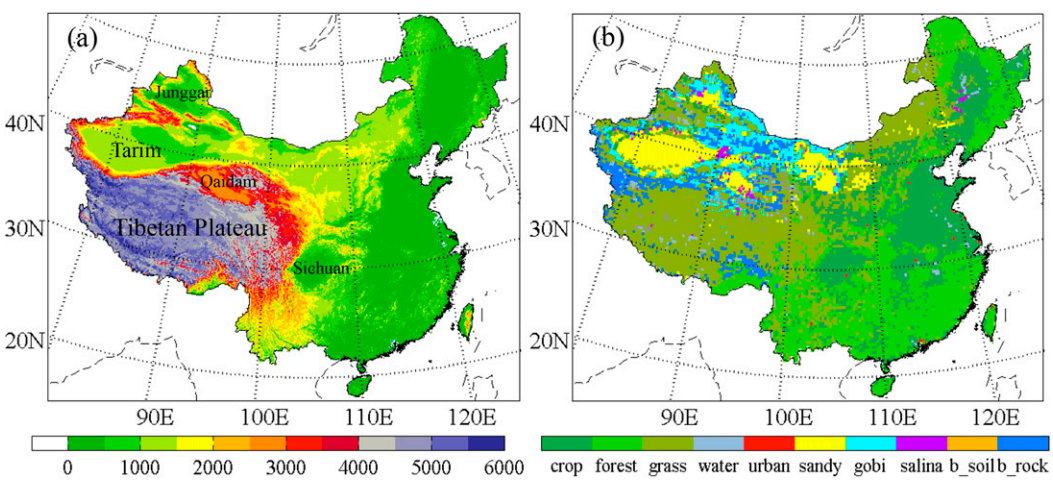

FIG. 2. Spatial distributions of (a) terrain height (m) and (b) surface type. The locations of the four basins surrounding the Tibetan Plateau are shown.

Brought to you by NOAA Central Library | Unauthenticated | Downloaded 01/30/24 04:02 PM UTC

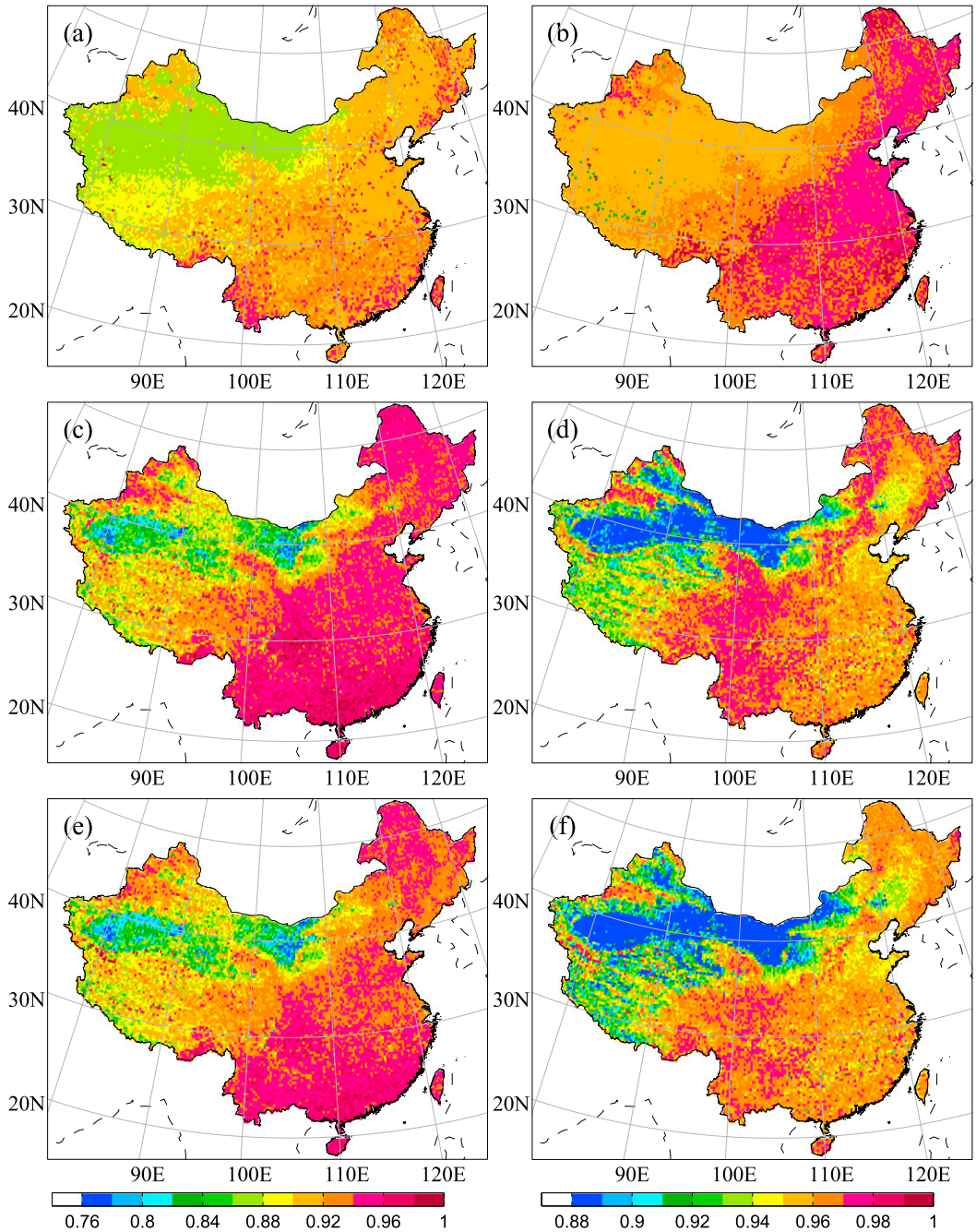

FIG. 3. (top) Spatial distributions of LSE from the IGBP dataset, (middle) UW_HSRemis in June, and (bottom) CAMEL_HSRemis in June for the (left) 3.9- and (right) 8.6-μm AHI channels.

Junggar, Tarim, Qaidam, and Sichuan basins. Eastern China is largely a plain with elevations lower than 1000 m.

The Multisource Integrated Chinese Land Cover Dataset, which was produced by the Chinese Academy of Sciences, combines the results from Landsat observations and intensive field surveys (Ran et al. 2010). The overall accuracy of the land-cover map was estimated to be 95%, which is the highest accuracy among all national-scale land-cover data products over China (Ran et al. 2012). In this dataset the nonvegetated surface is further divided into the following categories: sandy land, gobi, salina, bare soil, and bare rock. As seen from Fig. 2b, sandy lands are bordered by mountains and

Brought to you by NOAA Central Library | Unauthenticated | Downloaded 01/30/24 04:02 PM UTC

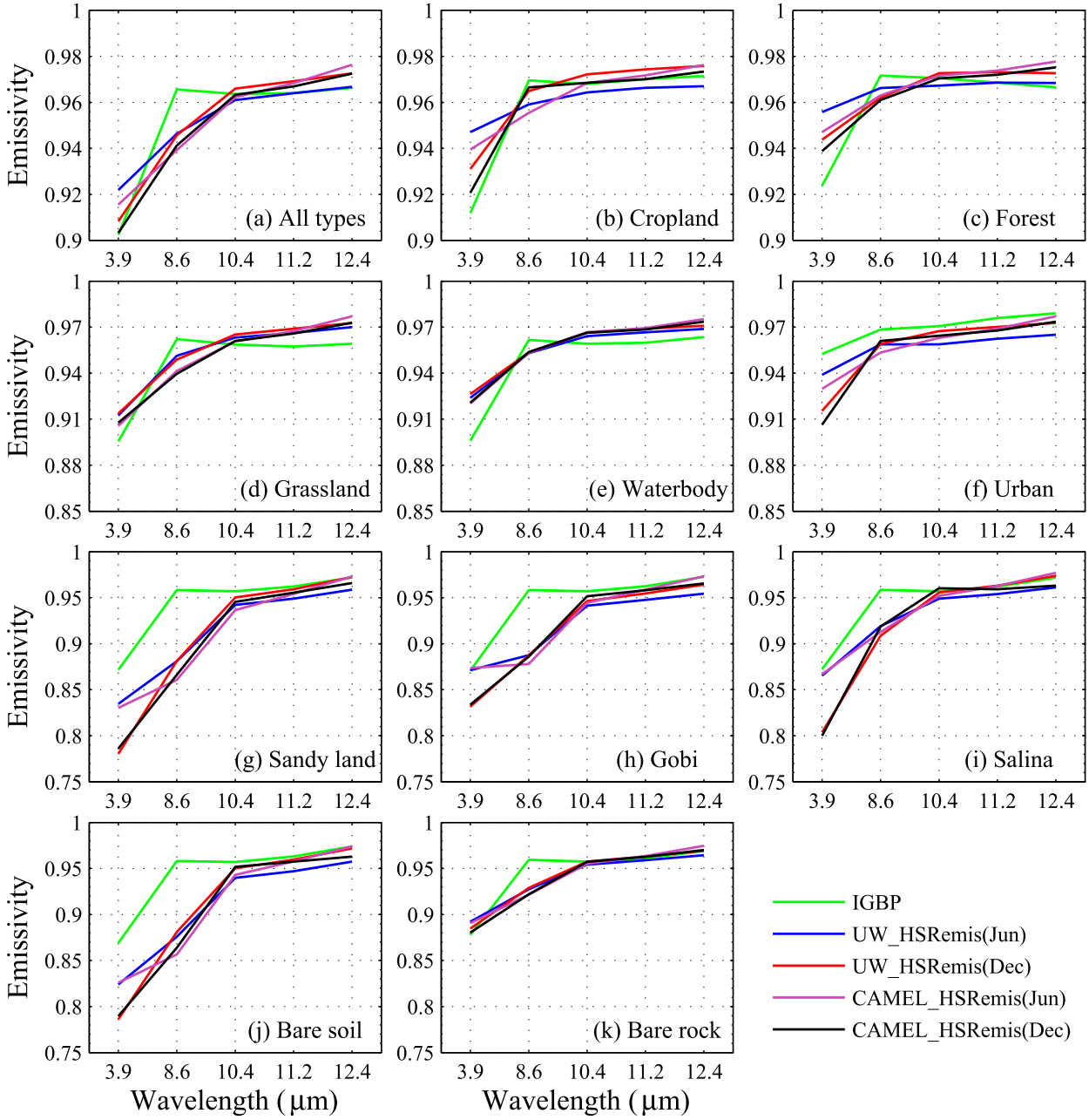

FIG. 4. Mean values of LSE averaged over (a) all surface types, (b) cropland, (c) forest, (d) grassland, (e) water body, (f) urban, (g) sandy land, (h) gobi, (i) salina, (j) bare soil, and (k) bare rock from different LSE datasets.

connected through the gobi and bare rock. Except for the sandy land in Inner Mongolia (~105°E, 40°N), all other sandy lands are located in the great basins.

3. Comparison of the three infrared LSE datasets

Figure 3 displays the spatial distributions of LSE from the IGBP dataset, which is independent of the month, and UW_HSRemis and CAMEL_HSRemis for the month of June at 3.9 and 8.6 μm. The LSE distributions from UW_HSRemis and CAMEL_HSRemis are similar. However, the IGBP LSE distribution is significantly different from the distributions of the other two LSE datasets. Over the nonvegetated area in northwestern China, the IGBP-derived LSE at 8.6 μm is higher than 0.95, but it goes as low as 0.88 for the UW_HSRemis- and CAMEL_HSRemis-derived LSEs. In eastern China, the LSE at 3.9 μm from the IGBP dataset is lower

Brought to you by NOAA Central Library | Unauthenticated | Downloaded 01/30/24 04:02 PM UTC

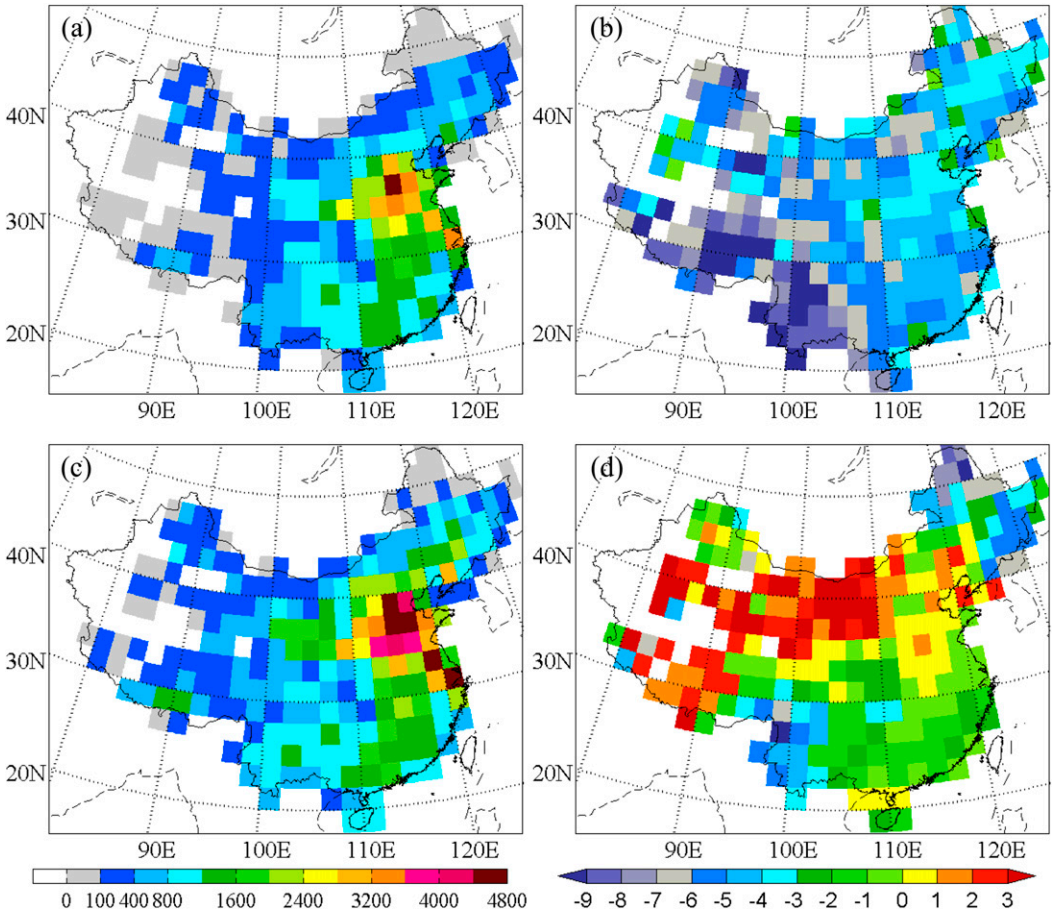

FIG. 5. (left) Spatial distributions of data counts and (right) mean differences in LST between ground-based observations and NCEP GFS analyses (K) averaged within 2° × 2° grid boxes during (a),(b) daytime and (c),(d) nighttime.

than that from UW_HSRemis and CAMEL_HSRemis, while the LSE at 8.6 μm from the IGBP dataset is higher than that from the two other datasets. Because of the limitation of the LUT approach, the IGBP LSE dataset does not capture spatial variations in a single surface type, while UW_HSRemis and CAMEL_HSRemis do.

Figure 4 presents the mean values of LSE from the IGBP dataset, as well as UW_HSRemis and CAMEL_HSRemis in June and December averaged over different surface types at the wavelengths of the five AHI surface-sensitive channels. For urban (Fig. 4f) and most nonvegetated surface types, including sandy land, gobi, salina, and bare soil (Figs. 4g–j), the IGBP LSE is consistently higher than the LSEs of UW_HSRemis and CAMEL_HSRemis within the entire infrared spectral range of 3.9–12.4 μm. For all vegetated surface types (Figs. 4b–d), and water body (Fig. 4e) and bare rock (Fig. 4k) surface types, the LSE values from the IGBP dataset are higher at 8.6 μm and lower at 3.9 μm. Within the 10.4–12.4-μm wavelength range, the three datasets are the most consistent for all surface types. The difference in LSE between UW_HSRemis and CAMEL_HSRemis is less than 0.02. Specifically, UW_HSRemis LSE values at 3.9 and 8.6 μm are slightly larger than those of CAMEL_HSRemis, while the LSE values at 10.4–12.4 μm from UW_HSRemis are slightly smaller than those of CAMEL_HSRemis. The differences between UW_HSRemis and CAMEL_HSRemis in June are larger than those in December. For each UW_HSRemis and CAMEL_HSRemis dataset, differences in LSE between June and December are small except for the LSE at 3.9 μm.

The largest differences among the three LSE datasets occur over nonvegetated surface types at 3.9 and 8.6 μm. Since the IGBP dataset does not differentiate the subsets of nonvegetated surface types—that is, sandy land, gobi, salina, bare soil, and bare rock—all of these surface types have the same IGBP-based LSE values of

Brought to you by NOAA Central Library | Unauthenticated | Downloaded 01/30/24 04:02 PM UTC

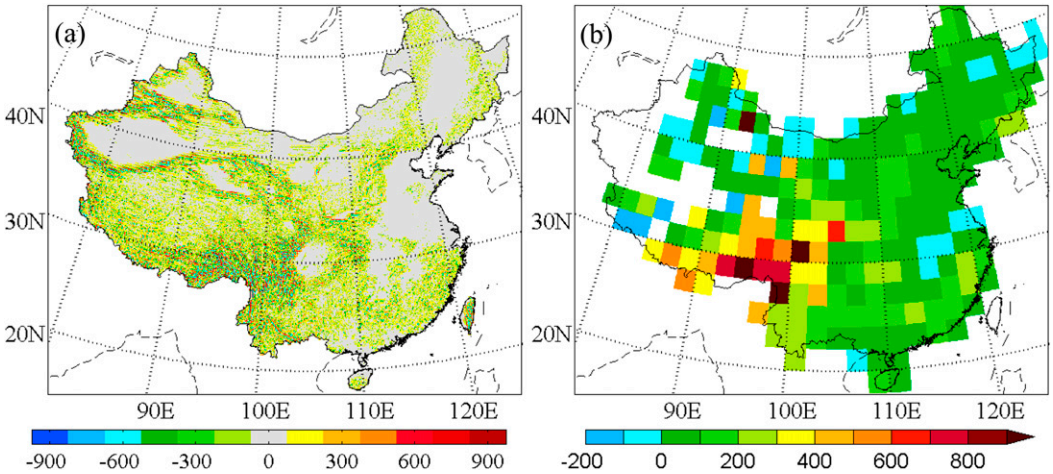

FIG. 6. Mean differences in terrain height (m) between 0.25° and 1-arc-min topography resolutions (a) for a 5-km Lambert grid and (b) interpolated at surface stations and then averaged to 2° × 2° grid boxes.

~0.88 at 3.9 μm and ~0.96 at 8.6 μm. However, both UW_HSRemis and CAMEL_HSRemis show that the LSE over sandy land and bare soil is about 0.05 lower than that over other nonvegetated surface types at 3.9 μm. The 3.9-μm LSE is about 0.78 in December and 0.84 in June for sandy land and bare soil. The LSE at 8.6 μm is less than 0.90 over all nonvegetated surface types except salina for UW_HSRemis and CAMEL_HSRemis. In addition, the 8.6-μm LSE from UW_HSRemis is higher than that from CAMEL_HSRemis over all nonvegetated surface types, which is consistent with the validations made by Borbas et al. (2017).

4. LST uncertainties in model forecasts

For most numerical weather prediction (NWP) models, the LST is not a prognostic variable that is explicitly predicted on model grid points, but it is derived from the following radiative balance equation (Zeng et al. 2012):

$$R_{\text{net}} = \varepsilon(\text{LW}_d - \sigma T_s^4) + \text{SW}_d(1 - \alpha), \qquad (2)$$

where T_S is the LST, SW_d is the downward shortwave radiative flux, LW_d is the downward longwave radiative flux, R_{net} is the net radiative flux, α is the surface albedo, ε is the broadband surface emissivity, and σ is the Stefan–Boltzmann constant; R_{net} is balanced by the sensible, latent, and ground heat fluxes. Therefore, the accuracy of LSTs from NCEP GFS analyses depends on the accuracy of the three heat fluxes and two radiative fluxes.

In this section the LSTs from NCEP GFS analyses are compared with direct ground-based observations of LSTs at the NBMO stations. Figure 5 shows the mean differences between NCEP GFS analyses and ground-based observations averaged within 2° × 2° grid boxes. The NCEP GFS LSTs have a significant cold bias during the day (Fig. 5b). The magnitude of the cold bias is ~4 K in eastern China and ~9 K in southwestern China. During nighttime the NCEP GFS LSTs show a warm bias in western China and a small cold bias in eastern China (Fig. 5d). A large cold LST bias is found near the southeastern edge of the Tibetan Plateau. The reasons why LSTs have such large uncertainties during the day (Fig. 5b) and night (Fig. 5d) are complicated.

First, the downward solar shortwave radiation used by the NCEP GFS model could have a negative bias during the daytime (Wang et al. 2014). If so, the first term on the right-hand side of Eq. (2) could be overestimated, resulting in a cold bias of NCEP GFS LSTs during the daytime.

Second, the LST difference may be affected by the horizontal resolutions of the model grids. A coarse grid configuration will smooth the steep terrain and introduce biases. Figure 6 shows the mean differences in terrain height between 0.25° and 1-arc-min topography resolutions (0.25° topography minus 1-arc-min topography). The 0.25° topography represents the terrain background used for the NCEP GFS analyses, while the 1-arc-min (~1 km) topography represents the actual terrain height. The absolute differences of the grid terrain heights at two separate resolutions can be as large as 900 m. Given a constant lapse rate of 7 K km^{-1}, the temperature difference associated with a terrain height error of 900 m would be greater than 6 K. The biases and standard deviations of LST differences between ground-based observations and NCEP GFS

Brought to you by NOAA Central Library | Unauthenticated | Downloaded 01/30/24 04:02 PM UTC

TABLE 2. Biases (μ) and standard deviations (σ) of LST differences between ground-based observations and NCEP GFS analyses interpolated at surface stations (analyses minus observations) when the differences in surface station terrain heights at two different resolutions [e.g., 0.25° topography minus 1-arc-min topography (Topo_Diff)] vary from less than −200 m to more than 500 m at 100-m intervals. The sample size (count) is also given.

Topo_Diff (m)	<−200	−200 to −100	−100 to 0	0 to 100	100 to 200	200 to 300	300 to 400	400 to 500	>500
Day									
μ	−4.21	−4.92	−4.00	−4.36	−5.30	−6.36	−6.78	−7.53	−7.65
σ	5.27	4.82	4.71	4.64	4.66	4.45	4.53	4.40	4.81
Count	747	1792	35 638	66 021	22 084	10 728	4661	2695	4690
Night									
μ	−0.83	0.26	0.42	0.02	−0.62	−1.45	−1.94	−1.75	−3.10
σ	3.98	3.93	3.70	3.89	3.96	3.91	4.16	4.64	4.74
Count	1385	2889	53 408	97 309	33 515	17 036	7972	5316	10 078

analyses interpolated to surface stations (analyses minus observations) are calculated at two different resolutions (Table 2). The magnitudes (i.e., the absolute values) of biases and standard deviations of LST differences increase as the height difference increases. When terrain height differences are less than 200 m, the LST differences during the nighttime are small; that is, the absolute values of the bias and the standard deviation are less than 1.0 and 4 K, respectively.

Third, there could also be deficiencies in the computation of sensible and ground heat fluxes over arid regions (Zheng et al. 2012; Trigo et al. 2015). The warm bias over sandy land could be caused by an underestimate of surface thermal conductivity, which is a key parameter in the computation of ground heat fluxes (Zeng et al. 2012). This explanation is verified by Table 3, where positive LST differences between ground-based observations and NCEP GFS analyses (analyses minus observations) are found over nonvegetated surfaces, including sandy land, gobi, salina, bare soil, and bare rock. A revised surface thermal conductivity may improve LST forecasts over nonvegetated regions.

Finally, it is worth mentioning that the LST has a large spatial variability that could lead to inconsistencies between model simulations and observations from surface stations. The LSTs from ground-based observations represent point measurements at the station location, while the LSTs from ECMWF analyses are averages in 0.25° × 0.25° grid boxes.

5. Impacts of infrared LSE on radiance simulations

Impacts of the infrared LSE on simulations of the five surface-sensitive AHI channels over different surface types are assessed based on the biases and standard deviations of brightness temperature between AHI observations (O) minus background simulations (B; OMBs). The radiance simulations are generated by the CRTMv2.2.3 with the three infrared LSE datasets previously discussed. To avoid having the bias in model-forecasted LST affect CRTM simulations, NBMO station-based LST observations are used instead of the NCEP GFS LST analyses as inputs to the CRTM. Using in situ point observations introduces an error in the representativeness between station observations and AHI infrared data. AHI data are aggregated to a kilometer-level grid center (2 km at nadir and ~4 km for China). The LST is expected to vary spatially, even in regions of apparent surface homogeneity. This representativeness issue is more significant during the daytime. Therefore, in this study daytime data are rejected, that is, data with solar zenith angles less than 90°. Furthermore,

TABLE 3. Biases (μ) and standard deviations (σ) of LST differences between ground-based observations and NCEP GFS analyses interpolated at surface stations (analyses minus observations) for different surface types. The sample size (count) is also given.

Surface type	Cropland	Forest	Grassland	Water body	Urban	Sandy land	Gobi	Salina	Bare soil	Bare rock
Day										
μ	−4.16	−5.60	−6.29	−4.65	−3.26	−5.02	−5.16	−3.16	−6.59	−6.93
σ	4.75	4.44	4.88	4.69	5.11	4.47	4.20	4.53	4.11	4.20
Count	91 355	32 863	17 734	500	84	1863	2171	289	7	994
Night										
μ	−0.05	−2.40	0.45	−0.23	−0.21	3.53	1.82	2.17	6.49	0.16
σ	3.63	3.49	4.78	4.65	2.29	4.00	4.21	3.13	2.58	4.57
Count	133 555	45 273	37 944	740	79	3365	3745	464	9	1882

Brought to you by NOAA Central Library | Unauthenticated | Downloaded 01/30/24 04:02 PM UTC

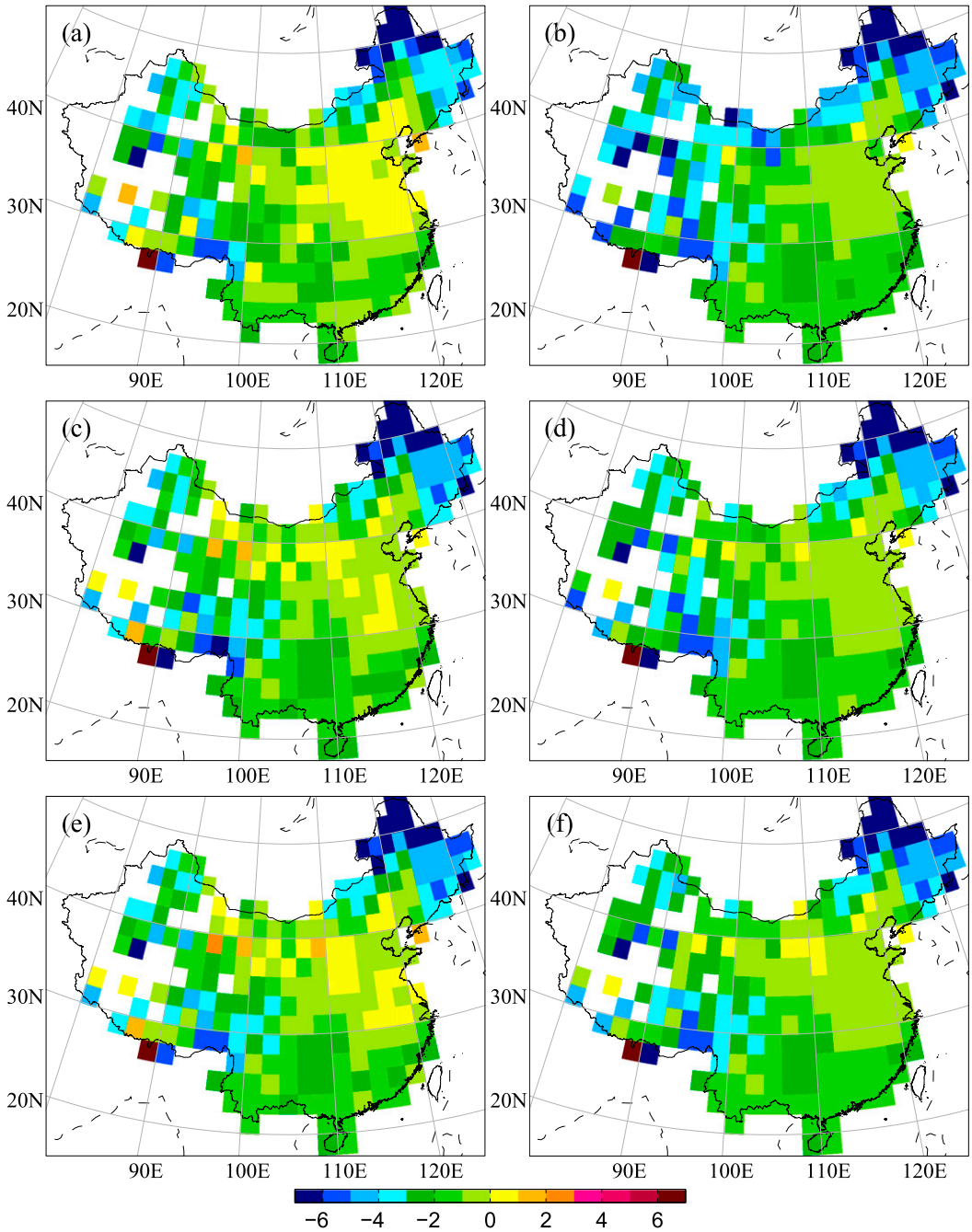

FIG. 7. Spatial distributions of brightness temperature OMB biases (K) for the (left) 3.9- and (right) 8.6-μm AHI channels within 2° × 2° grid boxes with model simulations generated using the LSE from the (top) IGBP dataset, (middle) UW_HSRemis, and (bottom) CAMEL_HSRemis.

data contaminated by clouds are excluded based on the AHI cloud mask described in section 2b. Finally, more than 220 000 data samples over 144 days are collected in the 2-yr period from July 2015 to June 2017. We have included data in different months to ideally include multiple seasons because for some areas, the clear-sky occurrence was predominant only for particular seasons. Figure 5c presents the spatial distributions of data counts within 2° × 2° grid boxes during the 144-day period. The sample size is small over the Tibetan Plateau, where NBMO stations are sparsely distributed. Northeastern China also has fewer samples because of cloud contamination.

Brought to you by NOAA Central Library | Unauthenticated | Downloaded 01/30/24 04:02 PM UTC

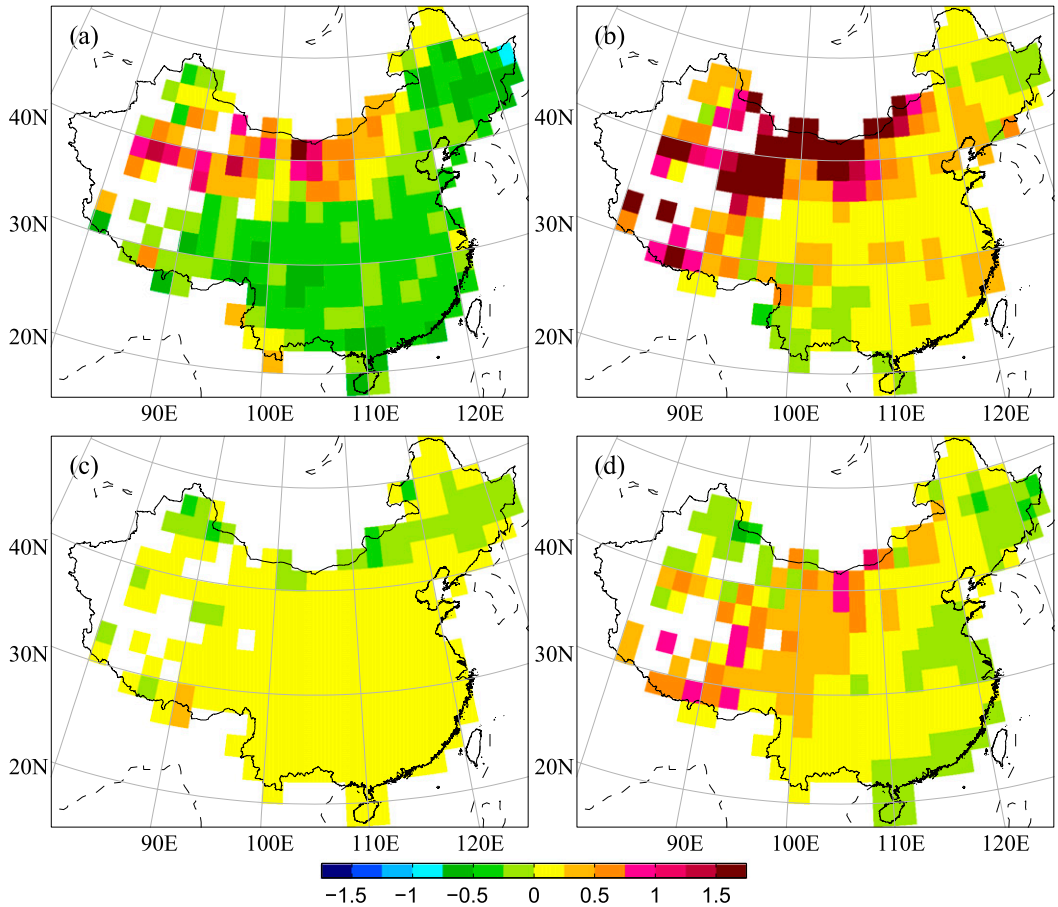

FIG. 8. Spatial distributions of the mean differences in brightness temperature simulations (K) for the (left) 3.9- and (right) 8.6-μm AHI channels (top) between IGBP and CAMEL_HSRemis, and (bottom) between UW_HSRemis and CAMEL_HSRemis.

Figure 7 shows the spatial distributions of AHI 3.9- and 8.6-μm OMB biases estimated using LSEs from the IGBP dataset, UW_HSRemis, and CAMEL_HSRemis as inputs to the CRTM. For both channels, the OMB biases are within the range of ±3 K for most of China, with larger differences predominant in areas with small sample sizes. A negative bias of less than −3 K for the AHI 8.6-μm channel is found in Xinjiang (~85°E, 40°N) and Inner Mongolia (~105°E, 40°N) for the IGBP LSE dataset (Fig. 7b). The biases at 8.6 μm are smaller, typically less than ±2 K, in the same area when the UW_HSRemis (Fig. 7d) and CAMEL_HSRemis (Fig. 7f) LSE datasets are used for model simulations. This is because the IGBP LSE at 8.6 μm is higher than that from both UW_HSRemis and CAMEL_HSRemis in northwestern China.

To show more clearly the differences in CRTM simulations of brightness temperature with different LSE datasets, Fig. 8 presents the spatial distributions of the mean differences in brightness temperature simulations for AHI channels at 3.9 and 8.6 μm between IGBP and CAMEL_HSRemis (Figs. 8a,b), and between UW_HSRemis and CAMEL_HSRemis (Figs. 8c,d). For the 3.9-μm channel, the differences between IGBP and CAMEL_HSRemis simulations can be as large as 1.5 K (Fig. 8a). Large positive differences are found over nonvegetated areas, while negative differences are found over eastern China. The differences in brightness temperature at 3.9 μm between the UW_HSRemis and CAMEL_HSRemis simulations are less than 0.25 K except for a few points (Fig. 8c). At 8.6 μm, the differences among the three simulations with different LSE datasets are small in eastern China and significantly large over nonvegetated surfaces. The differences between IGBP and CAMEL_HSRemis simulations (Fig. 8b) are typically larger than those between UW_HSRemis and CAMEL_HSRemis simulations (Fig. 8d), with the largest differences in nonvegetated regions.

The biases and standard deviations of OMBs estimated with different LSE datasets averaged over the

Brought to you by NOAA Central Library | Unauthenticated | Downloaded 01/30/24 04:02 PM UTC

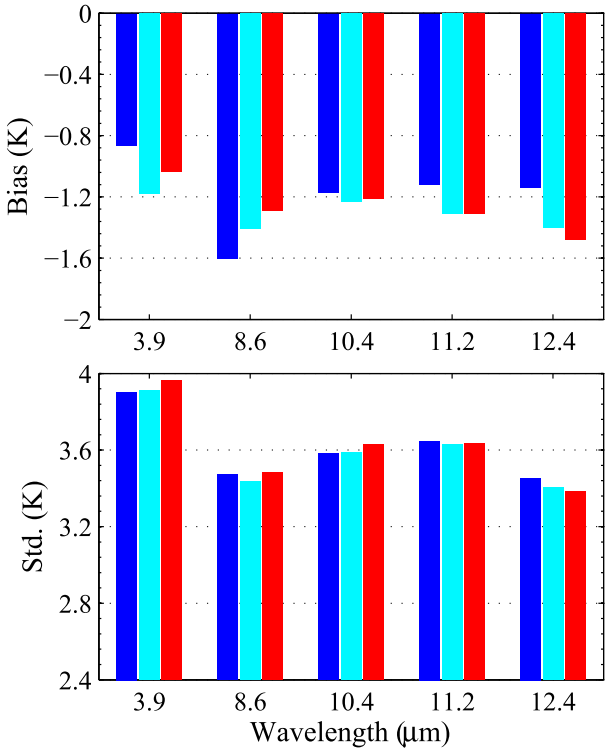

FIG. 9. (top) Biases and (bottom) standard deviations (Std) of brightness temperature OMBs for the five surface-sensitive AHI channels over the entire domain using the IGBP database (blue), UW_HSRemis (cyan), and CAMEL_HSRemis (red).

entire domain are provided in Fig. 9. The OMB biases are consistently negative. The simulations with the IGBP LSE dataset result in larger OMB biases (~1.6 K) for the 8.6-μm channel but smaller biases at the four other AHI channels, compared to those from the UW_HSRemis and CAMEL_HSRemis LSE datasets. The OMBs from the CAMEL_HSRemis LSE dataset have smaller negative biases for the 3.9- and 8.6-μm channels and larger negative biases for the 10.4-, 11.2-, and 12.4-μm channels, compared to those from UW_HSRemis. Note that the simulation biases include not only emissivity estimation errors but also brightness temperature and LST observation errors from AHI and NBMO stations, as well as systematic errors in the CRTM and NECP GFS analyses. Considering that the AHI observation error is ~0.3 K, as shown in Table 1, the differences in the biases of OMBs estimated with the UW_HSRemis and CAMEL_HSRemis LSE datasets are not significant at the five AHI surface-sensitive channels. The standard deviations of OMBs estimated with the three LSE datasets are largely consistent for all five surface-sensitive channels.

Figure 10 shows biases and standard deviations of brightness temperature OMBs for different surface types. Note that the results for the water body, urban, salina, and bare soil surface types are not included in Fig. 10 because of their small sample sizes (Table 3). The differences in OMB statistics estimated with the three LSE datasets are on average less than 0.3 K for cropland and forest types for all the AHI surface-sensitive channels, suggesting that the difference among the three datasets are not significant. Large differences (~0.8 K) occur for the grassland surface type at the 11.2- and 12.4-μm channels when comparing OMB results from the IGBP dataset to those from the UW_HSRemis and CAMEL_HSRemis datasets. Over the nonvegetated regions (i.e., sandy land, gobi, and bare rock), significant improvements occur at the 3.9- and 8.6-μm channels when the CAMEL_HSRemis dataset is used instead of the IGBP dataset. The improvements in brightness temperature simulations can be as large as 1.6 K at 8.6 μm for all three nonvegetated regions. There are no significant differences in OMBs among the three LSE datasets for the vegetated and nonvegetated surface types.

The seasonal dependence of OMB statistics is illustrated in Fig. 11 for the five AHI surface-sensitive channels over nonvegetated surface types. The differences between the IGBP simulations and those of the two other LSE datasets are the smallest in summer [June–August (JJA)]. By contrast, the differences are as large as 0.6 and 1.6 K at the 3.9- and 8.6-μm channels, respectively, in the other seasons [March–May (MAM); September–November (SON); December–February (DJF)]. This suggests a poorer performance of IGBP simulations because of a lack of LSE monthly variations.

6. Summary and conclusions

The accuracy of radiance simulations of satellite infrared surface-sensitive channels over land is greatly dependent on the specification of the LSE and LST. In this study two infrared LSE datasets—namely, UW_HSRemis and CAMEL_HSRemis—are incorporated into the CRTM and compared with the IGBP LSE dataset already embedded in the CRTM. The other key component—the LST—was improved by using NBMO station data to better capture the spatial heterogeneity for the multitude of surface conditions over China.

The UW_HSRemis and CAMEL_HSRemis LSEs have monthly variations, while the LSE in the IGBP dataset is fixed in time and varies with land classification. The IGBP LSE values are higher than those from the other two LSE datasets at the 8.6-μm wavelength. The 3.9-μm IGBP LSE is lower and higher than both the UW_HSRemis and CAMEL_HSRemis LSEs over

Brought to you by NOAA Central Library | Unauthenticated | Downloaded 01/30/24 04:02 PM UTC

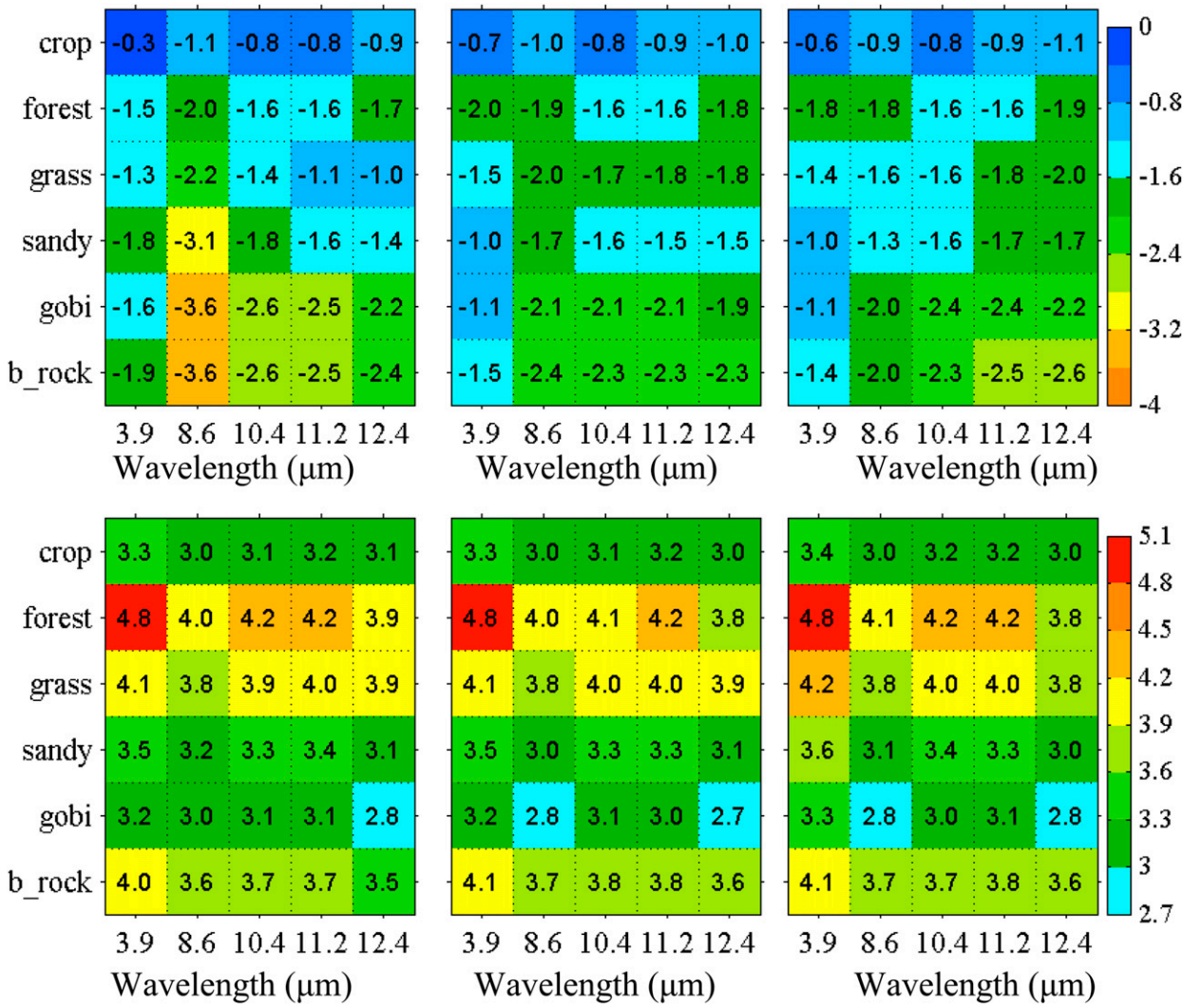

FIG. 10. (top) Biases (K) and (bottom) standard deviations (K) of brightness temperature OMBs for surface-sensitive AHI channels over different surface types with the (left) IGBP dataset, (center) UW_HSRemis, and (right) CAMEL_HSRemis. Note that statistical results for the water body, urban, salina, and bare soil surface types are not included because of too few data samples.

vegetated and nonvegetated surface types, respectively. The differences in LSE between UW_HSRemis and CAMEL_HSRemis are generally small with UW_HSRemis LSE values slightly larger at 3.9 and 8.6 μm and smaller within the 10.4–12.4-μm wavelength range than CAMEL_HSRemis LSE values.

These differences in LSEs affected the radiance simulations of AHI surface-sensitive channels. The simulation accuracies with the three LSE datasets are compared by examining fits to AHI observations for nighttime scenes over China using the CRTM with background fields from NCEP GFS analyses and LST observations from the NBMO stations in China. Considering the brightness temperature and LST observation errors from AHI and NBMO stations, and systematic errors in the CRTM and NECP GFS analyses, the differences in simulation biases with the three LSE datasets are not significant over cropland and forest surface types. For the grassland surface type, the CRTM simulations with the IGBP dataset have the smallest bias at 10.4, 11.2, and 12.4 μm compared with biases from simulations using the other two LSE datasets. For nonvegetated surface types, such as sandy land, gobi, and bare rock, the CRTM simulations with the IGBP dataset are poorer than those using the UW_HSRemis and CAMEL_HSRemis datasets at 3.9 and 8.6 μm. The standard deviations of simulation biases are comparable between the three LSE datasets. When examining the seasonal variation of simulation biases, differences between simulation biases from the IGBP

Brought to you by NOAA Central Library | Unauthenticated | Downloaded 01/30/24 04:02 PM UTC

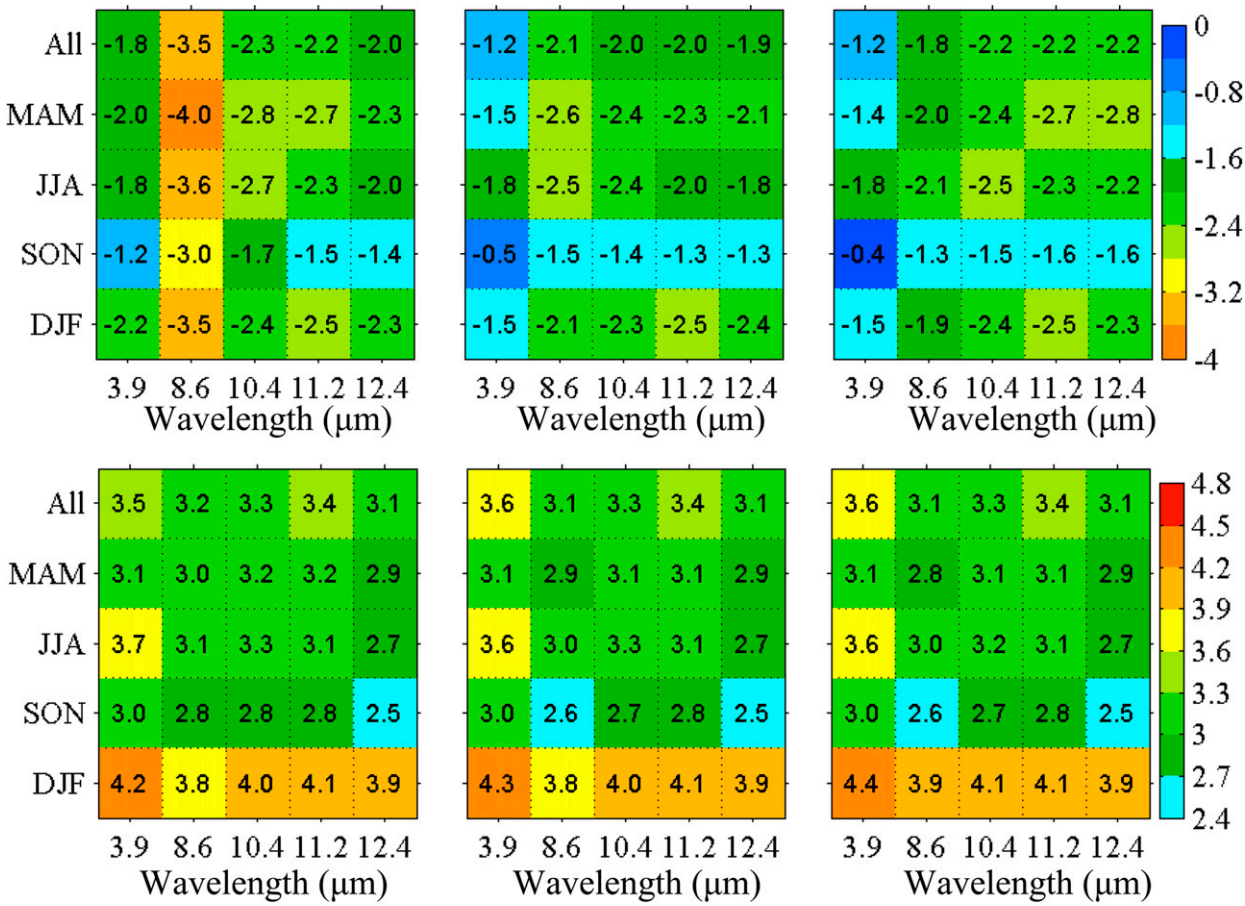

FIG. 11. (top) Biases (K) and (bottom) standard deviations (K) of brightness temperature OMBs for surface-sensitive AHI channels over nonvegetated types (i.e., sandy land, gobi, and bare rock) for different seasons with the (left) IGBP dataset, (center) UW_HSRemis, and (right) CAMEL_HSRemis.

dataset and those from the other two datasets are smallest in summer and more significant in the other three seasons. Thus, improvements in simulating AHI infrared surface-sensitive channels can be made when using spatially and temporally varying LSE estimates. In fact, the infrared LSE varies greatly with respect to surface material, soil moisture content, and vegetation-cover characteristics (van de Griend and Owe 1993). A more accurate LSE dataset could be retrieved from satellite observations or simulated in land surface models by considering the effects of vegetation and soil parameters.

In the past two decades, satellite measurements of infrared water vapor sounding channels have been assimilated in NWP models over both land and ocean, but those of infrared surface-sensitive channels are assimilated only over oceans (Köpken et al. 2004; Zou et al. 2011, 2015). The latter is mainly due to the large uncertainties of model simulations over land. This study therefore contributes to assimilations of AHI surface-sensitive channels in NWP models over land or AHI environmental data record products involving model simulations. Obtaining accurate radiance simulations is only the first step toward the assimilation of AHI surface-sensitive channels over land. Cloud detection, bias correction, and quality control are other components that are also important for the successful assimilation of AHI surface-sensitive channels over land. These areas will be investigated in several follow-on studies. It is hoped that in the near future, AHI surface-sensitive channels over land will finally contribute to an improved NWP forecast skill through AHI data assimilation as was done over oceans (Qin et al. 2017).

Acknowledgments. This research work was jointly supported by the National Key R&D Program of China (Grant 2017YFC1501603), the National Natural Science Foundation of China (Grant 41505086), the National Oceanic and Atmospheric Administration GOES-R Program (Grant NA14NES4320003), and the National

Brought to you by NOAA Central Library | Unauthenticated | Downloaded 01/30/24 04:02 PM UTC

Fundamental Research 973 Programs of China (Grant 2015CB452800). We thank Dr. Eva Borbas at UW for providing the CAMEL_HSRemis and UW_HSRemis datasets, and Dr. Youhua Ran at the Chinese Academy of Sciences for providing the Multisource Integrated Chinese Land Cover Dataset.

REFERENCES

Bessho, K., and Coauthors, 2016: An introduction to Himawari-8/9—Japan's new-generation geostationary meteorological satellites. *J. Meteor. Soc. Japan*, **94**, 151–183, https://doi.org/10.2151/jmsj.2016-009.

Borbas, E. E., and B. C. Ruston, 2010: The RTTOV UWiremis IR land surface emissivity module. Version 1, NWP SAF Mission Rep. NWPSAF-MO-VS-042, 24 pp., https://nwpsaf.eu/vs_reports/nwpsaf-mo-vs-042.pdf.

——, R. O. Knuteson, S. W. Seemann, E. Weisz, L. Moy, and H.-L. Huang, 2007: A high spectral resolution global land surface infrared emissivity database. *Joint 2007 EUMETSAT Meteorological Satellite Conference and the 15th Satellite Meteorology & Oceanography Conference of the American Meteorological Society*, EUMETSAT P.50, 5 pp.

——, G. Hulley, R. Knuteson, and M. Feltz, 2017: MEaSUREs Unified and Coherent Land Surface Temperature and Emissivity (LST&E) Earth System Data Record (ESDR): The Combined ASTER and MODIS Emissivity Database over Land (CAMEL). NASA Tech. Doc., 30 pp., https://lpdaac.usgs.gov/sites/default/files/public/product_documentation/cam5k30_v1_user_guide_atbd.pdf.

Chen, W., 2005: *Satellite Meteorology*. China Meteorological Press, 521 pp.

Chen, Y., Y. Han, P. Van Delst, and F. Weng, 2010: On water vapor Jacobian in fast radiative transfer model. *J. Geophys. Res.*, **115**, D12303, https://doi.org/10.1029/2009JD013379.

Han, Y., F. Weng, Q. Liu, and P. van Delst, 2007: A fast radiative transfer model for SSMIS upper atmosphere sounding channels. *J. Geophys. Res.*, **112**, D11121, https://doi.org/10.1029/2006JD008208.

Hulley, G. C., S. J. Hook, E. Abbott, N. Malakar, T. Islam, and M. Abrams, 2015: The ASTER Global Emissivity Dataset (ASTER GED): Mapping Earth's emissivity at 100 meter spatial scale. *Geophys. Res. Lett.*, **42**, 7966–7976, https://doi.org/10.1002/2015GL065564.

Köpken, C., G. Kelly, and J.-N. Thépaut, 2004: Assimilation of Meteosat radiance data within the 4D-Var system at ECMWF: Assimilation experiments and forecast impact. *Quart. J. Roy. Meteor. Soc.*, **130**, 2277–2292, https://doi.org/10.1256/qj.02.230.

Li, Z., J. Li, X. Jin, T. J. Schmit, E. E. Borbas, and M. D. Goldberg, 2010: An objective methodology for infrared land surface emissivity evaluation. *J. Geophys. Res.*, **115**, D22308, https://doi.org/10.1029/2010JD014249.

Qin, Z., X. Zou, and F. Weng, 2017: Impacts of assimilating all or GOES-like AHI infrared channels radiances on QPFs over Eastern China. *Tellus*, **69**, 1345265, https://doi.org/10.1080/16000870.2017.1345265.

Ran, Y., X. Li, and L. Lu, 2010: Evaluation of four remote sensing based land cover products over China. *Int. J. Remote Sens.*, **31**, 391–401, https://doi.org/10.1080/01431160902893451.

——, ——, ——, and Z. Li, 2012: Large-scale land cover mapping with the integration of multi-source information based on the Dempster–Shafer theory. *Int. J. Geogr. Inf. Sci.*, **26**, 169–191, https://doi.org/10.1080/13658816.2011.577745.

Salisbury, J. W., A. Wald, and D. M. D' Aria, 1994: Thermal-infrared remote sensing and Kirchhoff's law: 1. Laboratory measurements. *J. Geophys. Res.*, **99**, 11 897–11 911, https://doi.org/10.1029/93JB03600.

Seemann, S. W., E. E. Borbas, R. O. Knuteson, G. R. Stephenson, and H.-L. Huang, 2008: Development of a global infrared emissivity database for application to clear sky sounding retrieval from multispectral satellite radiances measurements. *J. Appl. Meteor. Climatol.*, **47**, 108–123, https://doi.org/10.1175/2007JAMC1590.1.

Takahashi, M., 2016: Inter-calibration of Himawari-8/AHI using CrIS as a reference. *GSICS Users' Workshop*, College Park, MD, NOAA, 18 pp., http://gsics.atmos.umd.edu/pub/Development/UsersWorkshop2016/AhiIrCal_2016GUW_Takahashi.pptx.

Trigo, I. F., S. Boussetta, P. Viterbo, G. Balsamo, A. Beljaars, and I. Sandu, 2015: Comparison of model land skin temperature with remotely sensed estimates and assessment of surface-atmosphere coupling. *J. Geophys. Res. Atmos.*, **120**, 12 096–12 111, https://doi.org/10.1002/2015JD023812.

van de Griend, A. A., and M. Owe, 1993: On the relationship between thermal emissivity and the normalized difference vegetation index for nature surfaces. *Int. J. Remote Sens.*, **14**, 1119–1131, https://doi.org/10.1080/01431169308904400.

Vogel, R. L., Q. Liu, B. Ruston, Y. Han, and F. Weng, 2010: A new infrared land surface emissivity database for the Community Radiative Transfer Model. *Sixth Annual Symp. on Future National Operational Environmental Satellite Systems-NPOESS and GOES-R*, Atlanta, GA, Amer. Meteor. Soc., 7.2, https://ams.confex.com/ams/90annual/techprogram/paper_163052.htm.

Walker, J. R., W. M. MacKenzie, J. R. Mecikalski, and C. P. Jewett, 2012: An enhanced geostationary satellite–based convective initiation algorithm for 0–2-h nowcasting with object tracking. *J. Appl. Meteor. Climatol.*, **51**, 1931–1949, https://doi.org/10.1175/JAMC-D-11-0246.1.

Wang, A., M. Barlage, X. Zeng, and C. S. Draper, 2014: Comparison of land skin temperature from a land model, remote sensing, and in situ measurement. *J. Geophys. Res. Atmos.*, **119**, 3093–3106, https://doi.org/10.1002/2013JD021026.

Weng, F., 2007: Advances in radiative transfer modeling in support of satellite data assimilation. *J. Atmos. Sci.*, **64**, 3799–3807, https://doi.org/10.1175/2007JAS2112.1.

Zeng, X., Z. Wang, and A. Wang, 2012: Surface skin temperature and the interplay between sensible and ground heat fluxes over arid regions. *J. Hydrometeor.*, **13**, 1359–1370, https://doi.org/10.1175/JHM-D-11-0117.1.

Zheng, W., H. Wei, Z. Wang, X. Zeng, J. Meng, M. Ek, K. Mitchell, and J. Derber, 2012: Improvement of daytime land surface skin temperature over arid regions in the NCEP GFS model and its impact on satellite data assimilation. *J. Geophys. Res.*, **117**, D06117, https://doi.org/10.1029/2011JD015901.

Zhuge, X., and X. Zou, 2016: Test of a modified infrared-only ABI cloud mask algorithm for AHI radiance observations. *J. Appl. Meteor. Climatol.*, **55**, 2529–2546, https://doi.org/10.1175/JAMC-D-16-0254.1.

——, and ——, 2018: Summertime convective initiation nowcasting over southeastern China based on Advanced Himawari Imager observations. *J. Meteor. Soc. Japan*, https://doi.org/10.2151/jmsj.2018-041, in press.

——, ——, and Y. Wang, 2017a: A comparison between three surface type data sets adopted by the Community Radiative

Brought to you by NOAA Central Library | Unauthenticated | Downloaded 01/30/24 04:02 PM UTC

Transfer Model. *Remote Sens. Lett.*, **8**, 801–810, https://doi.org/10.1080/2150704X.2017.1328142.

——, ——, and ——, 2017b: A fast cloud detection algorithm applicable to monitoring and nowcasting of daytime cloud systems. *IEEE Trans. Geosci. Remote Sens.*, **55**, 6111–6119, https://doi.org/10.1109/TGRS.2017.2720664.

Zhuo, H., Y. Liu, and J. Jin, 2016: Improvement of land surface skin temperature simulation over the Tibetan Plateau and the associated impact on circulation in East Asia. *Atmos. Sci. Lett.*, **17**, 162–168, https://doi.org/10.1002/asl.638.

Zou, X., Z. Qin, and F. Weng, 2011: Improved coastal precipitation forecasts with direct assimilation of *GOES-11/12* imager radiances. *Mon. Wea. Rev.*, **139**, 3711–3729, https://doi.org/10.1175/MWR-D-10-05040.1.

——, ——, and Y. Zheng, 2015: Improved tropical storm forecasts with *GOES-13/15* imager radiance assimilation and asymmetric vortex initialization in HWRF. *Mon. Wea. Rev.*, **143**, 2485–2505, https://doi.org/10.1175/MWR-D-14-00223.1.

——, X. Zhuge, and F. Weng, 2016: Characterization of bias of Advanced Himawari Imager infrared observations from NWP background simulations using CRTM and RTTOV. *J. Atmos. Oceanic Technol.*, **33**, 2553–2567, https://doi.org/10.1175/JTECH-D-16-0105.1.

Brought to you by NOAA Central Library | Unauthenticated | Downloaded 01/30/24 04:02 PM UTC